Remote Sensing Of Environment
October 2021, Volume 264 Pages 112614 (13p.)
https://doi.org/10.1016/j.rse.2021.112614
https://archimer.ifremer.fr/doc/00709/82117/

Assessment of ocean wave spectrum using global Envisat/ASAR data and hindcast simulation

Li Huimin [1, 3, *], Stopa Justin [2], Mouche Alexis [3], Zhang Biao [1], He Yijun [1], Chapron Bertrand [3]

[1] School of Marine Sciences, Nanjing University of Information Science and Technology, Nanjing, China
[2] Department of Ocean and Resources Engineering, University of Hawaii at Manoa, Honolulu, HI, USA
[3] Ifremer, Univ. Brest, CNRS, IRD, Laboratoire d'Océanographie Physique et Spatiale (LOPS), IUEM, Brest, France

* Corresponding author : Huimin Li, email address : huimin.li@nuist.edu.cn

Abstract :

Wave mode of spaceborne synthetic aperture radar (SAR) is designed for the global ocean wave observations. Despite the fact that the significant wave height inferred from SAR measurements has been validated against model output and in-situ data, SAR's primary and unique capability for operational 2-dimensional spectral description of sea state remains to be fully evaluated. In this study, we extended the previous assessment approaches by introducing a new SAR image spectral parameter, the Mean rAnge Cross-Spectrum (MACS) that focuses on the isolated wave scales along the radar line-of-sight direction. MACS is an efficient variable in that it characterizes the local wave spectra properties without need of the non-linear wave inversion procedure. The assessment is based on the multiple-year data acquired by Envisat/ASAR wave mode, along with the collocated WaveWatch III (WW3) hindcast and the in-situ buoy-observed wave spectra, for which the SAR forward transformation is systematically performed to obtain the simulated image spectra. Inter-comparison between SAR-measured and WW3-simulated MACS demonstrates that the consistency is wavelength (or wavenumber) dependent. Three typical wavelengths, around 62 m for windsea, 168 m for intermediate waves and 342 m for swell, are selected to present the MACS comparison in detail. Comparable magnitude of SAR-measured and the simulated MACS is observed for the intermediate waves and swell, while larger simulation values are predicted for the windsea waves. Spatial distribution of MACS agrees well between these two data sets for all wavelengths with high correlation coefficients (>0.8) in most of the global ocean. One exception is in the extratropics where the quantitative difference is particularly notable. In the contrary, when comparing SAR-measured and buoys-simulated MACS, the agreement increases towards the shorter (<100 m) wavelengths. We also found that the large-scale atmospheric/oceanic features persistent on SAR images lead to the overestimate of SAR MACS at long wavelengths, which is expected to bias the wave inversion. The wave spectra retrieval performance shall advance as long as such impact is properly resolved.

Highlights

► A novel assessment approach of SAR wave measurement is proposed using MACS. ► The long-time Envisat/ASAR observations is compared with model outputs and buoy. ► The MACS comparison shows the consistency is wavelength dependent. ► MACS shall validate the capability of SAR in resolving wave spectral information.

Keywords : Envisat/ASAR wave mode observations, SAR image spectral parameter, Spectral assessment

1. Introduction

Sea state information is crucial to managing ocean resources and safe operations for ocean going activities. Global wave information has been paramount in understanding wind and wave patterns including regional variability (Young, 1999). Significant wave heights are accurately measured by satellite altimetry within a precision of 10-20 cm with regard to *in-situ* buoy observations (Queffeulou, 2004; Zieger et al., 2009). These data have greatly helped the development, calibration, and validation of numerical spectral wave models with improved predictability (Ardhuin et al., 2010; Stopa et al., 2016b). While this information is important to monitor regional change (Young et al., 2011), they are not sufficient to fully represent the wave conditions, particularly for multimodal wave systems. Active radars, such as real aperture radars (RAR) and synthetic aperture radars (SAR) are the operational spaceborne sensors to measure both wavelength and wave directions on global scales. Of which, SAR is advantageous owing to its high spatial resolution that allows to resolve the wind waves as well as the long-time series since the 1990s.

A SAR emits microwave pulses and precisely measure their Doppler-shifted returns. Since the ocean surface is in continuous motion, the radar returns are often misplaced when converting from Doppler-frequency to geo-referenced images in space. The misplacement leads to nonlinear distortions of wave signatures in the along-track direction referred to as the azimuth cutoff (Kerbaol et al., 1998). When the local wind forcing is calm to moderate, the azimuth cutoff wavelength is usually shorter than the swell components, enabling to uniquely estimate both wavelength, direction and spectral energy of swell systems with SAR (Collard et al., 2009; Ardhuin et al., 2017). On the other hand, the high frequency waves are often distorted. This has motivated several empirical studies to directly estimate significant wave height (SWH) from SAR images using statistical methods (Schulz-Stellenfleth et al., 2007; Stopa and Mouche, 2017; Quach et al., 2020). However, the direction and wavelength information is lost especially for waves smaller than the azimuth cutoff which is typically 150-200 m. (Li and Saulter, 2012) compared the subrange SWH integrated over distinct wave scales, rather than the overall SWH of advanced-SAR (ASAR) aboard Envisat satellite relative to buoys and models. Their approach in (Li and Saulter, 2012) validates SAR observations in terms of the subrange wave height, but relies on the operational quasi-linear inversion scheme employed by ESA since ERS (Krogstad et al., 1994). It is worth noting that such a scheme is not able to fully recover the nonlinear distortions (Krogstad et al., 1994). So far, the validations of SAR observations regarding ocean wave spectral retrieval are based on either total or effective SWH. The inversed wave spectra has not yet been assessed in terms of their spectral features relative to the reference data.

In the cross-track direction (range) of SAR image coordinate, the distortion is less strong and the mapping could be approximated as a quasi-linear process. The Mean RAnge Cross-Spectra (MACS) introduced by (Li et al., 2019) has shown its reliability in describing up to 20 m range-traveling waves Sentinel-1 (S-1) C-band SAR. MACS offers opportunities to investigate the wave information of isolated wave scale in the range direction without going through a non-linear SAR inversion scheme or performing the hypothesis of a quasi-linear imaging mechanism. As a complementary study to the SWH assessment (Li and Saulter, 2012), we attempt to evaluate the wave spectral signatures through MACS of ASAR observations with respect to wave spectral model output and *in-situ* buoy measurements. Using this approach can potentially lead to a better understanding of the wave dynamics while assessing the SAR and spectral wave model, WAVEWATCH3 (WW3) (The WAVEWATCH III® Development Group). In order to carry out the comparison of MACS between SAR and WW3/buoy, we implement the nonlinear forward SAR mapping transformation in (Engen and Johnsen, 1995) for given ocean wave spectra and SAR configurations to obtain the simulated SAR image spectra. In this study, following the general assessment strategy of integral wave height (Young, 1999; Li and Saulter, 2012), the quantitative relationship of MACS parameter for various wavelengths is examined between WW3-simulation and SAR measurements. The global signatures of SAR MACS relative to the simulation is also investigated and discussed to highlight their spatial consistency. An independent comparison with buoy observations is invoked to further interpret the inter-comparison results between ASAR and the collocated WW3-simulation.

Specifically in this study we use the two-dimensional wave spectra simulated from a hindcast (Stopa et al., 2019) and measured by buoys to derive equivalent MACS values to compare with Envisat/ASAR observations from 2002-2012. We take benefit of this entire decade of SAR data to statistically compare MACS obtained at various wavelengths and at global scale. The manuscript is organized as follows. In section 2 we describe the data sets and methodology: forward SAR transformation and MACS definition. In section 3, we present the MACS comparison between ASAR measurements and the simulation from the WW3 hindcast and buoy ocean wave spectra. Discussions and conclusions follow in Sections 4 and 5, respectively.

2. Data and MACS definition

In this section, we first describe the Envisat/ASAR data and wave spectra from the numerical wave model. Next we describe the forward SAR transformation used to map wave spectra into an equivalent image cross-spectra. Lastly we describe the estimation of MACS from the SAR image cross-spectra.

2.1. Envisat/ASAR wave mode

Envisat/ASAR operated for nearly a decade from November 2002 to April 2012. It is a C-band radar (center frequency of 5.4 GHz), collecting SAR images in various modes. Wave mode is dedicated to observing global ocean waves (Hasselmann et al., 2012). SAR images are acquired every 100 km along the track, having spatial footprint of 10×7 km (azimuth by range) with spatial resolution of 9×6 m. In this work, we use wave mode images at incidence angle of 23° in VV polarization. Envisat is a polar orbit satellite, with both ascending (flying from South Pole to the North Pole) and descending trajectories. To concentrate on a consistent wave direction and monitor its global feature, only the data acquisitions from the ascending passes are included in this study with a total number of SAR images around 3×10^6.

The Level-1B products of SAR image cross-spectrum are systematically processed from the single look complex (SLC) SAR images. Each image spectrum is composed of 24 discrete wavenumbers ranging from 0.008 rad·m^{-1} to 0.2 rad·m^{-1} and 36 direction (Johnsen, 2005). The images acquired between January 2007 and April 2012 are collocated with the operational ECMWF

(European Centre for Medium-Range Weather Forecasts) analysis wind vectors (Nagarajan and Aiyyer, 2004). The reanalysis product is available at spatial resolution of 0.5° every 6h (0h,6h,12h,18h). The wind vector at the nearest spatial and temporal point to the SAR passing time is taken as the reference wind of each SAR image.

2.2. Hindcast ocean wave spectra

The wave spectra are generated from version 5.16 of the spectral wave model WAVEWATCH3, hereinafter WW3 (The WAVEWATCH III® Development Group). We use the parameterizations of wave generation and dissipation proposed by (Ardhuin et al., 2010) and the non-linear Discrete Interaction Approximation by (Hasselmann and Hasselmann, 1985). It has been shown that this model configuration works well for H_s and swell partitions in comparison to other parameterization packages (Stopa et al., 2016a). The global model is implemented at latitude and longitude grid of 0.5° with a spectral bin composed of 24 directions and 32 frequencies that are exponentially spaced from 0.037 Hz to 0.7 Hz at an increment of 10%. The wind and ice fields at spatial resolution of 0.2° (22 km) from the Climate Forecast System Reanalysis (CFSR) (Saha et al., 2010, 2014) are used to force the model runs. The hindcast was calibrated and corrected in time to match a homogenized satellite altimetry database of (Queffeulou and Croizen-Fillon) (Stopa, 2018; Stopa et al., 2019).

We output the wave spectra directly for each longitude, latitude, and time corresponding to the Envisat/ASAR acquisition. The minimum wavelength of WW3 wave spectra is 3.2 m (0.7 Hz), smaller than the wave mode resolution (9 m). This would ensure that all wavelengths resolved by SAR are comparable with WW3 wave spectra.

2.3. Buoy observations

The wave measurements from National Data Buoy Center (NDBC) are used in this study as complementary to SAR observations and model outputs. A triple collocation data set is created by limiting the spatial distance between the center of SAR images within 100 km and the temporal window shorter than 30 mins. It ends up with 1263 collocation pairs.

The wave spectra measured by NDBC buoys, is composed of frequency from 0.04 Hz up to 0.4850 Hz (Vandemark et al., 2005). We employed the Maximum Entropy Method (MEM) proposed in (Lygre and Krogstad, 1986) to reconstruct the two-dimensional wave spectra from estimates of the Fourier coefficients. In specifics, this includes $\alpha 1$ that represents the mean wave direction, $\alpha 2$ that denotes the dominant wave direction, and $r1$ and $r2$ that describe the directional spreading relative to the main direction. The directional bin for buoy wave directional spectral reconstruction is set to be 10 $^{\circ}$ throughout rest of this paper unless otherwise stated.

2.4. SAR forward transformation

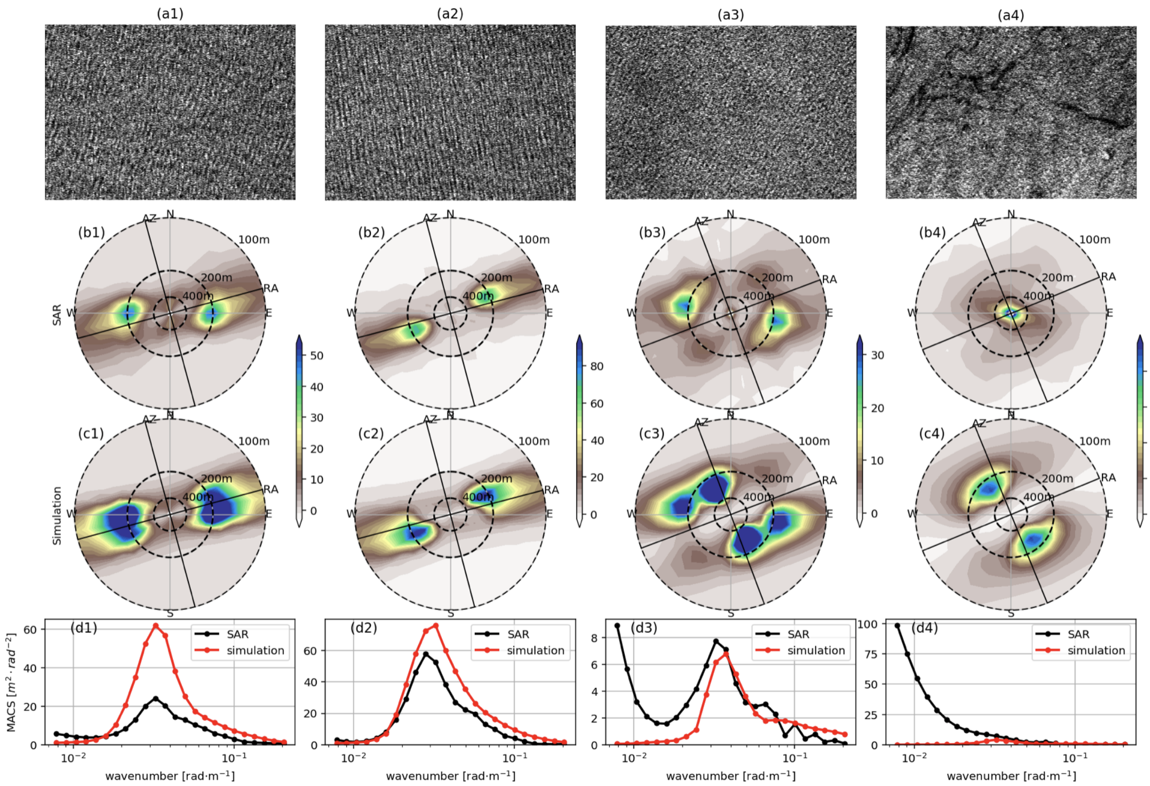

Figure 1: Examples of ENVISAT/ASAR wave mode images for definition of range MACS profile. The row (a1)-(a4) shows the SAR backscattering image. Real component of the SAR cross-spectra is given in the second row (b1)-(b4) and the corresponding simulated cross-spectra using WW3 wave spectra and the forward SAR transformation is in the third row (c1)-(c4). The polar plots of the cross spectra show the wavelength in circles from inner to the outer are 400 m, 200 m and 100 m, respectively. The bottom row (d1)-(d4) shows the MACS profile representing the energy for wavenumbers along the range direction.

The SAR forward transformation maps the wave spectra into SAR image cross-spectra, which is calculated using two sub-looks during the SAR integration time. The imaginary component is associated to wave motion within the time difference between the two sub-looks. It is therefore widely used to reduce the 180° direction ambiguity of the swell propagation (Engen and Johnsen, 1995). In addition, the cross spectra helps filter non-coherent signals typically improving the signal-to-noise ratio of ocean waves.

(Engen and Johnsen, 1995) presented detailed derivation of SAR image cross-spectra using the general formula for nonlinear mapping:

$$P_S^{mn}(\vec{k}, \Delta t) = \int d\vec{x}\; e^{-i\vec{k}\cdot\vec{x}}\; e^{k_x^2[\rho_{aa}(\vec{x},t)-\rho_{dd}(\vec{0},0)]}[1 + \rho_{II}(\vec{x}, t)] \tag{1}$$

where the subscript a and I in ρ_{aa} denote the velocity bunching and real aperture radar (RAR) modulation, respectively. k_x is the wavenumber along the azimuth direction. The correlation function defined in Eq. (1) is related to the ocean wave spectrum $S(\vec{k})$ through

$$\rho_{aa}(\vec{x}, \Delta t) = \frac{1}{(2\pi)^2} \int d\vec{k}\; e^{i\vec{k}\cdot\vec{x}} \cdot \frac{1}{2}\left[\left|M_a(\vec{k})\right|^2 e^{-i\omega\Delta t} S(\vec{k}) + \left|M_a(-\vec{k})\right|^2 e^{i\omega\Delta t} S(-\vec{k})\right] \tag{2}$$

where M_a represents the modulation transfer function (MTF) for RAR or velocity bunching. The detailed formulation of MTF can be found in (Engen and Johnsen, 1995; Li et al., 2019). In this study, we use the real component of SAR image cross-spectra for MACS.

Four SAR roughness images acquired by Envisat/ASAR wave mode are shown in Figure 1 (a1)-(a4). Real component of the measured SAR and simulated WW3 cross spectra are then accordingly given in (b1)-(b4) and (c1)-(c4). In general, the most energetic wave systems appear to agree between SAR and WW3 image spectra. Despite the matched spectral pattern, WW3 has overall larger values for the dominant waves. Note that in panel (b3)&(c3), a wave system along SAR azimuh direction is predict by WW3, but not well resolved by SAR observations. Also, though it is likely that the non-ocean waves patterns inducing large-scale modulation as observed in panel (a4) impacts the cross-spectral analysis, its quantitative influence still needs to be further investigated.

2.5. *MACS profile extraction*

In this manuscript, we follow the procedure of (Li et al., 2019) to compute MACS from both observations and simulations by

$$MACS(k) = \frac{1}{N}\int_A P_s(k,\phi), \qquad A \in [\phi_{ra} - 10^\circ < \phi < \phi_{ra} + 10^\circ] \tag{3}$$

where $P_s(k,\phi)$ represents the cross-spectrum in polar coordinate. ϕ_{ra} is SAR range direction. In this study, we extend our range of wave scales from 47 m to 800 m. The smallest wavelength is 47 m because ASAR range spatial resolution is about 9 m and we use a factor of ≈5 to ensure the waves are properly resolved by the Fourier Transform. The range profile (±15° relative to the line-of-sight) of SAR image cross-spectra is thus extracted, denoted as MACS profile hereinafter. Figure 1 bottom row shows the MACS profiles for these four representative cases. The overall MACS wavenumber distributions generally match, but there are noticeable differences in magnitude. In panel (d1) and (d2), simulated MACS profiles have larger values than observations. In panel (d3), the SAR exhibits higher MACS energy for wavelengths longer than 400 m. While in panel (d4), SAR MACS is constantly larger for the wavelengths longer than 150 m. This is clearly due to the presence of the large-scale phenomenon as observed in the SAR image. MACS can be computed for any wavelength between 30 m and 800 m with ASAR. Hereinafter, we denote as MACS_λ where λ is the wavelength. For example MACS_{62}, represents MACS for wavelengths of 62 m.

3. Results

In this section, we examine the consistency of MACS profile between SAR-observations and WW3-simulations. Taking advantage of the versatility of MACS, we analyze the statistical relationship as well as the global patterns of MACS for three different wavelengths of 62.5 m, 168.4 m and 342.0 m. We also carried out MACS comparisons with external wave measurements by buoys as an attempt of interpreting the differences found between SAR and WW3-simulation.

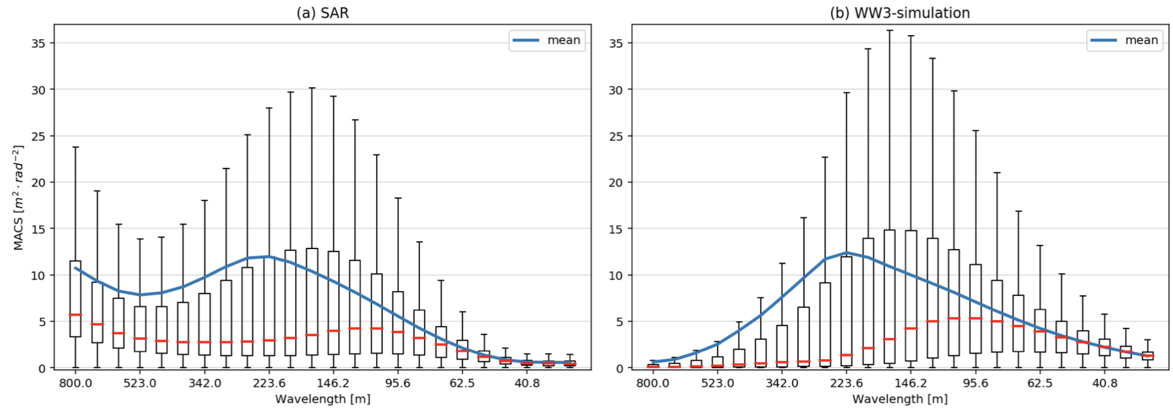

Figure 2: Box plot of MACS profile from (a) SAR-observation; (b) WW3-simulation with respect to wavelength. For MACS at given wavelength, each rectangle spans the first quartile to the third quartile (the interquartile range, IQR). The red segment inside rectangles denotes the median. The upper whisker extends to the largest data value within $1.5 \times IQR$ above the third quartile and the lower to the smallest value within $1.5 \times IQR$ below the first quartile. The blue curve represents the mean for each wave scale.

3.1. MACS profile

MACS profile of SAR-observation and WW3-simulations between January 2007 and April 2012 is presented in box plot relative to wavelength in Figure 2. The central box represents the likely range of variation : the interquartile range, IQR. The whisker extends to the largest and smallest data value within $1.5 \times IQR$ from the lower and upper quartile, respectively. MACS profile of SAR shares a couple of commonality with that of WW3-simulation. First, for most of the wavelengths, MACS is not normally distributed as the distance of the median to the upper quartile is much larger than that to the lower quartile. In other words, MACS is generally right-skewed with smaller median (red segment) than the mean (blue curve). The mean and median are largely apart except over shorter wavelengths (<62.5 m) where these two are almost identical. The profile peak also differs as the mean locates at 223.6 m and the median at 95.6 m. The maximum IQR locates at wavelength of 168.4 m, different from both the median and the mean. Despite the resembling distributions of MACS for each wave scales between SAR and WW3, they also differ in several aspects. SAR MACS profile in Figure 2(a) has a clear increase towards longer wavelengths beyond 523.0 m for mean, median and IQR. While WW3-simulation shows consistent MACS decrease towards both longer and shorter wavelengths from the peak. Both data sets have comparable mean MACS except for the very long wavelengths. It is not the case for the median and IQR. For wavelengths shorter than 250 m, the WW3-simulated IQR is larger than SAR-observations. As for the median, the WW3 exceeds at wavelength shorter than 146 m. The distribution of WW3-simulated MACS at one particular wavelength roughly follows a negative exponential function, while the SAR-observed is a log-normal curve (not shown). In any case, smaller IQR suggests a less spread distribution. On the other hand, for wavelengths longer than 250 m, the slow variation of SAR MACS might result from the impact of large-scale oceanic and atmospheric phenomena as displayed in Figure 1(a4)-(d4). This also possibly results in the large spread of SAR MACS than the WW3-simulation.

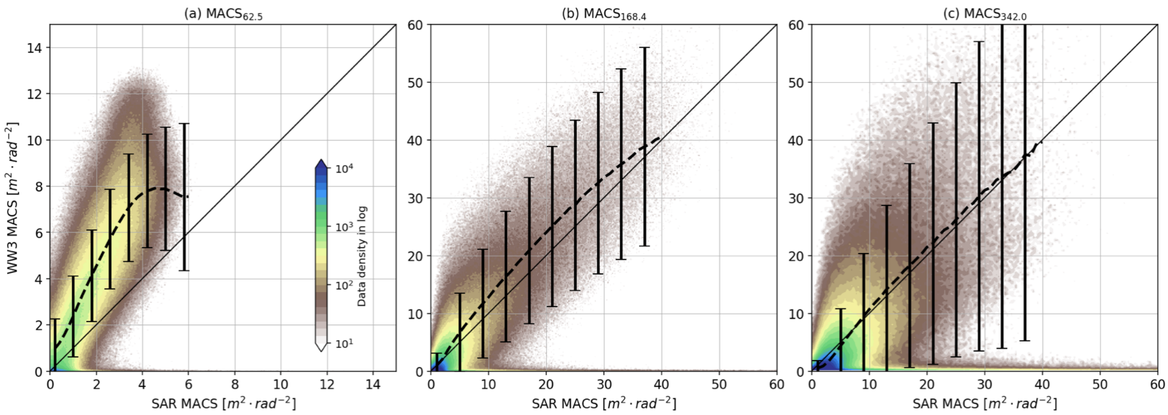

Figure 3: Q-Q plot of MACS comparison between SAR and WW3-simulation for three wavelengths (a)62.5 m; (b)168.4 M; (c)342.0 m. The dashed lines are the mean curve and the error bar stands for the one standard deviation. Color denotes data count in log scale.

Going further, we now focus on observed and simulated MACS for short (62.5 m), intermediate (168.4 m) and long (342.0 m) waves. Wavelength of 168.4 m has both comparable mean and median between SAR and WW3. MACS of 62.5 m exhibits smaller values in SAR observations than WW3 simulations, while it is the opposite trend for MACS of 342.0 m. The Q-Q plots of SAR MACS relative to the simulated MACS for these three selected wavelengths are presented in Figure 3. For 62.5 m as shown in Figure 3(a), WW3-simulation is consistently higher than that of SAR with data points well above the one-to-one line. If we neglect the saturation of SAR MACS beyond 4 $m^2 \cdot rad^{-2}$, slope of the linear fit to these points approximates 2. It means that for most of SAR acquisitions, the predicted MACS by WW3 is twice larger than the SAR observations. With wavelength of 168.4 m shown in Figure 3(b), the agreement improves as most of the data points scatter around the one-to-one line. It should be noted that the mean curve (dashed line) slightly deviates from a linear variation. While for wavelength of 342.0 m in Figure 3(c), the mean curve is indeed well following the one-to-one curve. However, the MACS relationship is largely dispersed as represented by the larger standard deviation. For the $MACS_{342.0}$, its standard deviation gradually increases with $MACS_{342.0}$ values. For the other two wavelengths, the standard deviation is almost constant from small to large MACS values. In particular, very small MACS values are predicted by WW3-simulation as shown by the large number of data points clustered close to the horizontal axis in Figure 3(c). The spatial consistency between these two data sets is yet to be confirmed. As such, the comparison of global MACS for these three selected wavelengths are analyzed in the following.

3.2. Spatial analyses of MACS

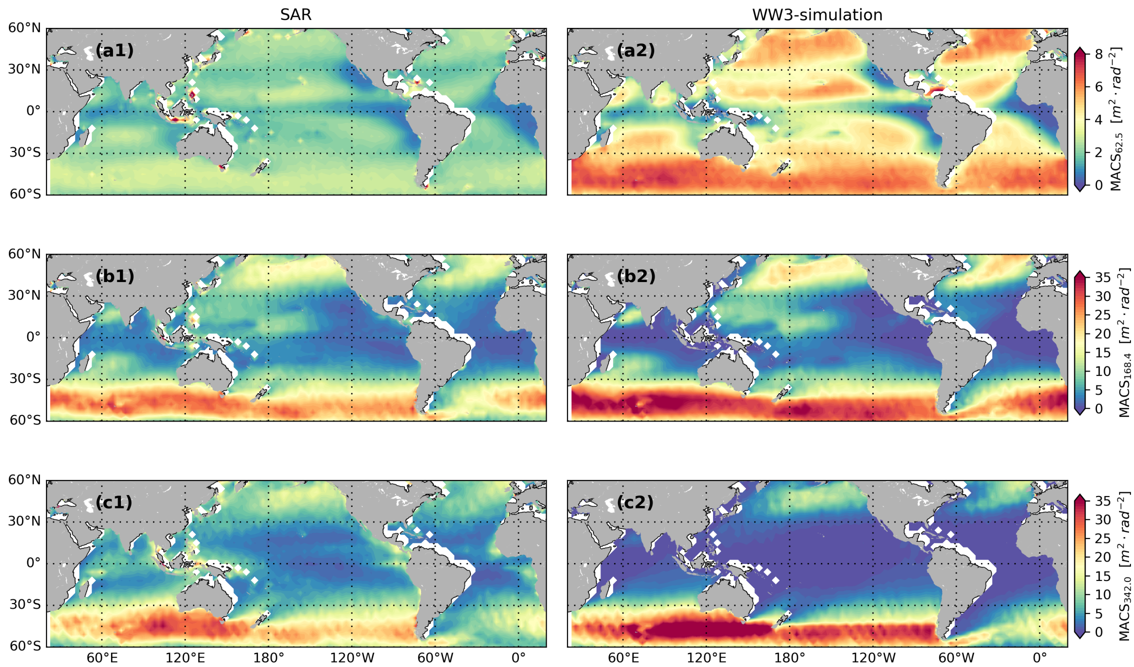

Figure 4: Global average of MACS from (left) SAR and (right) WW3-simulation for (top) 62.5 m; (middle) 168.4 m and (bottom) 342.0 m. Both latitude and longitude are binned into 2.5° by 2.5°. The bins located 50 km from the closest land are masked by blank space. Color denotes magnitude of MACS and note that the color bar dynamics differ in the three panels.

We also compute global maps of the three representative $MACS_{62.5}$, $MACS_{168.4}$, and $MACS_{342.0}$ to describe short, intermediate and long wavelengths. In qualitative terms, the global patterns of

SAR-observed and WW3-simulated MACS are similar. Average of global MACS at wavelength of 62.5 m from SAR-observations (left) and WW3-simulations (right) is given in top panel of Figure 4. The spatial features both mimic that of the overall wind field (Young, 1999) as these short waves are closely coupled with moderate wind speeds around 7 $m \cdot s^{-1}$ (Hasselmann et al., 1973). Smaller $\mathrm{MACS}_{62.5}$ are observed over the Inter Tropical Convergence Zone (ITCZ) corresponding to the low wind speed throughout the year (Žagar et al., 2011). Over the extratropics, larger $\mathrm{MACS}_{62.5}$ is caused by the high wind events associated to the frequent low-pressure storm activities. However, the SAR-observed MACS is systematically smaller than the WW3-simulated values across the globe, consistently with Figures 2 and 3(a). For example, in the Southern Ocean, WW3-simulated $\mathrm{MACS}_{62.5}$ is around 6 $m^2 \cdot rad^{-2}$, which is twice as large as the SAR-observed $\mathrm{MACS}_{62.5}$. Such trend of smaller SAR-observed MACS exists for all the wavelengths up to 150 m (not shown here for brevity). MACS of these two data sets becomes gradually closer as the wavelength increases to approximately 170 m (see Figure 2).

We show $\mathrm{MACS}_{168.4}$ in the middle panel of Figure 4. Overall, WW3-simulated and SAR-observed $\mathrm{MACS}_{168.4}$ are in good agreement in terms of the global pattern. Similar to $\mathrm{MACS}_{62.5}$, $\mathrm{MACS}_{168.4}$ is also consistently high (around 25 $m^2 \cdot rad^{-2}$) throughout the year in the southern extratropics. The trade wind regions have reduced MACS in comparison to the extra-tropical regions. Yet, quantitative differences remain. Overestimates of the simulated MACS mainly locate in the extratropics, contrast to the global trend of $\mathrm{MACS}_{62.5}$. Note that over the Arabian Sea, this overestimate is also evident during the monsoon season (seasonality not shown). It is thus speculated that WW3-simulation tends to predict larger spectral energy for 168.4 m waves at relatively high wind conditions. At low to median wind speed, the relative magnitude depends on geographic loctions. For example, SAR-observed $\mathrm{MACS}_{168.4}$ generally exceeds the simulation in the East Equatorial Pacific Ocean. While in the Tropics, SAR-observed $\mathrm{MACS}_{168.4}$ has larger values. This spatial pattern well corresponds to the feature presented in Figure 3(b). Larger WW3-simulated $\mathrm{MACS}_{168.4}$ is mostly observed at larger MACS values, in other words at high sea state, like in the extratropics. While the larger SAR-observed $\mathrm{MACS}_{168.4}$ mostly occurs at smaller MACS values as depicted by the blue cluster in Figure 3(b).

At last, global average of $\mathrm{MACS}_{342.0}$ is displayed in the bottom panel of Figure 4. It is expected that this longer wavelength relates to wind speeds approximately equivalent to 18 ms^{-1} (Hasselmann et al., 1973). Large MACS$_{342.0}$ values are mostly located in the extratropics, particularly in the Southern Hemisphere. Given the duration and fetch needed for the long waves to grow, MACS$_{342.0}$ are mostly observed in the east part of the Pacific and Atlantic Ocean, distinguished from the spatially distributed MACS for short wavelengths. The South America shelters the MACS$_{342.0}$ in the South Atlantic. In the trade wind regions, the WW3-simulations have similar regional patterns as the SAR observations but with much lower magnitude. While in the extratropics, WW3-simulation exhibit larger MACS values throughout the year. This results in the scattered comparison and large standard deviation in Figure 3(c).

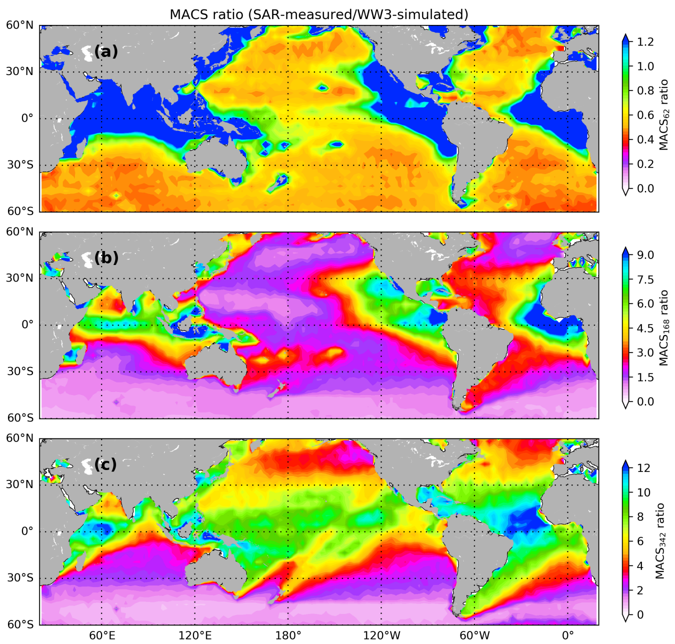

Figure 5: Global magnitude difference of MACS (simulation-SAR) for (a)62.5 m; (b) 168.4 m; (c) 342.0 m . The latitude/longitude bin of 2.5° is used in this figure.

To further assess the difference in the geographical pattern, we first computed the MACS magnitude difference (WW3-SAR) as shown in Figure 5. The magnitude difference is uniformly positive for MACS$_{62.5}$ across the globe in Figure 5(a). This corresponds to the constantly larger WW3-simulation as presented in both Figure 3 (left panel) and Figure 4 (top panel). With increasing wavelength, MACS difference shows significant spatial variability. For example, both MACS$_{168.4}$ and MACS$_{342.0}$ have much higher positive values in the southern extratropics than the rest of the global surface in Figure 5(b) and (c), respectively. In the contrary, $MACS_{342.0}$ difference is negative in the trade winds regions due to the smaller WW3-simulation as observed in Figure 4 bottom panel. It is worth noting that the straight boundary line at latitude of $45°S$ in both Figure 5(b) and (c) are present throughout the year. Investigations of this abrupt alignment change will be further addressed.

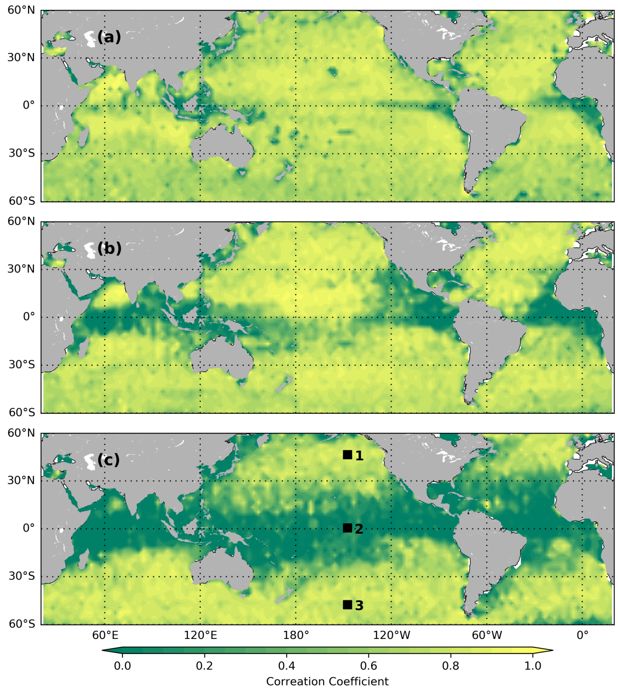

Figure 6: Global correlation coefficients of MACS between SAR measurements and WW3-simulation for (a) 62.5 m; (b) 168.4 m; (c) 342.0 m. The latitude/longitude bin of 2.5° is used in this figure. The three black rectangle indicate the areas selected for detailed correlation analysis in the following.

The Pearson correlation coefficients for MACS at 62.5 m, 168.4 m and 342.0 m are calculated from the monthly time series over each latitude/longitude bin of 2.5°, and shown in Figure 6. As in Figure 6(a), $MACS_{62.5}$ between the two data sets is highly correlated with correlation coefficient larger than 0.8 in most of the open ocean. Similarly, $MACS_{168.4}$ has strong correlation on the global scale, except over a narrow band at the equator (±10°) where the correlation coefficient decreases to 0.1 as in Figure 6(b). The low correlation along the equator extends to the entire trade winds region, reaching ±30°for $MACS_{342.0}$ as in Figure 6(c).

To further analyze the location dependent correlations, three areas of each covering 5° in both

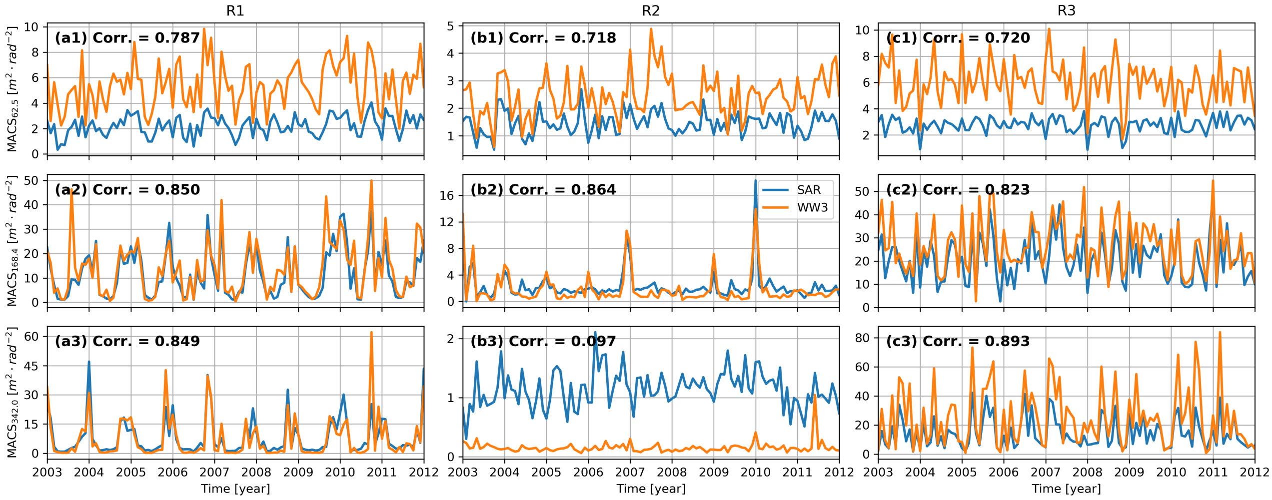

Figure 7: Time series for MACS over the three areas annotated in Figure 6, from left to right are R1, R2 and R3, respectively. For each area, from top to bottom are 62.5 m, 168.4 m and 342.0 m. The correlation coefficient is accordingly given in each plot.

latitude and longitude are selected and annotated by black rectangle in Figure 6(c). The monthly time series of MACS for 62.5 m, 168.4 m and 342.0 m over each area are then plotted in top, middle and bottom panel of Figure 7, respectively. The variation trend of temporal $MACS_{62.5}$ is found similar for both data sets except that WW3-simulation has consistently larger values. Despite that the simulated and observed MACS differentiate approximately by a factor of 2 over the time period, the co-variation results in the correlation coefficients higher than 0.70 for all these three areas. While for $MACS_{168.4}$ in the middle row, both data sets show comparable variation trends as well as quantitative values. Ocean waves of 168.4 m is better resolved by wave mode than the 62.5 m because they are less subject to the accuracy of input winds. This produces the high correlations (>0.80) found for all three areas. Contrast to the shorter wavelength in Figure 7(a1), MACS in (a2) exhibits much stronger seasonal changes. In winter, long ocean waves are generated by the high wind events associated with the winter storms and the averaged $MACS_{168.4}$ reaches up to 25 $m^{-2} \cdot rad^{-2}$. As the winter storms recede, the winds lowers and $MACS_{168.4}$ accordingly reaches the minimum values in summer close to zero. For the long waves of $MACS_{342.0}$, both R1 and R3 see consistent variation of SAR observation and WW3-simulation. Note that the WW3-simulation is greatly underestimated over R2 as shown in Figure 7(b3), resulting in the lower correlation coefficient of 0.097. This agrees well with the negative MACS difference in Figure 5(c). We attributed this discrepancy to the pollution of SAR-observed MACS by atmospheric or air-sea interaction features, including rain impact and wind streaks et al. In fact, high occurrence of such phenomena has been detected by the automatic classification of Sentinel-1 SAR wave mode data Wang et al. (2019) and particularly in the Tropics.

3.3. *Triple comparison with buoy measurements*

The global signatures of MACS strongly resemble for both data sets. Meanwhile it is found that the WW3-simulation is generally larger than the SAR MACS. This quantitative difference also depends on the spatial locations at the globe. Taking advantage of the numerous Envisat/ASAR acquisitions, a triple comparison between SAR, WW3 and buoy measurements is carried out to further diagnose the difference between these data sets.

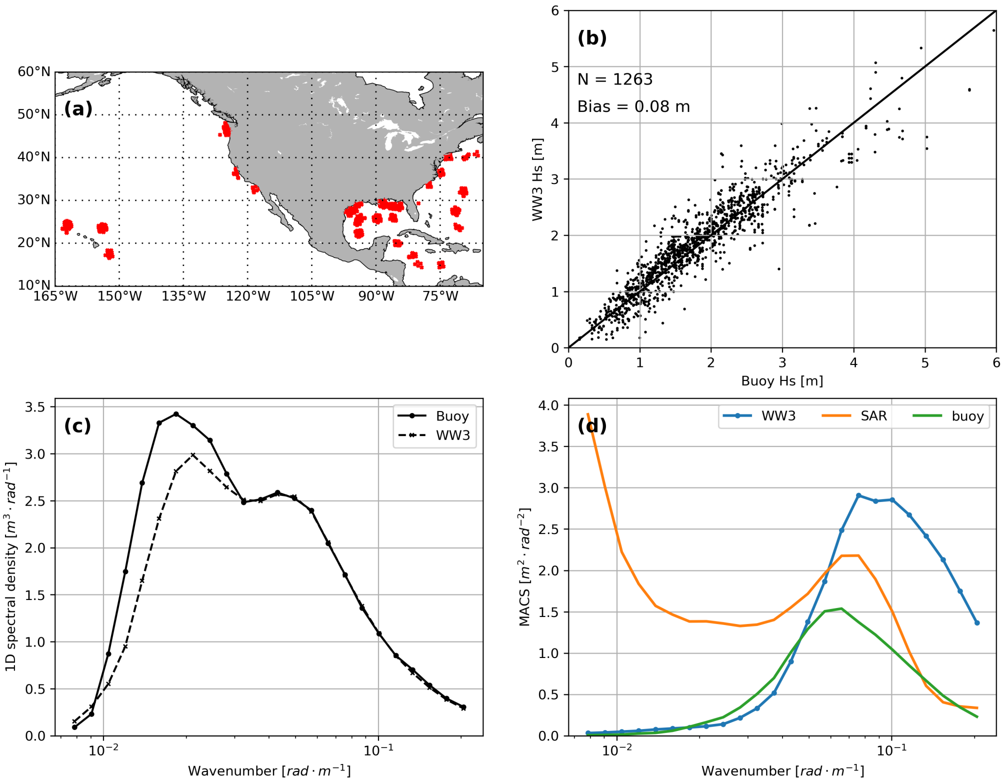

Figure 8: Comparison of triple collocation between SAR, buoy and WW3. (a) Position of NDBC buoys included in this study. (b) Comparison of significant wave height between collocated WW3 and buoys. (c) One-dimensional wave spectra from buoy and WW3. (d) The averaged MACS profile over all collocation pairs.

To extend the inter-comparison with *in-situ* measurements, the NDBC wave buoys that are capable of obtaining two-dimensional wave spectra are collocated with the Envisat/ASAR wave mode data set. This ends up with 1218 collocated data points. The spatial positions of these collocated wave buoys are shown in Figure 8(a). Of which, 714 collocated data points are scattered in the Gulf of Mexico and 64 points off the west coast and the rest (443 points) are around the Hawaii. We first compared the significant wave height of both buoys and WW3, which are in good consistency with negligible biases. The averaged one-dimensional wave spectra from all buoys measurements with corresponding WW3 simulations are then given in Figure 8(b). Both data sets present high conformity for most of the wavelengths, except at the long waves of 350 m where buoy tends to measure slightly larger wave spectral density. The two wave peaks are well captured by WW3 and buoys. One is long swell (wavelength of 330 m) coming from remote storms in the Southern Ocean and the north extratropics. The other corresponds to locally generated wind sea at wavelength of 120 m. This comparison well evidences the capability of WW3 in accurately modelling the one-dimensional ocean wave spectra.

However, the MACS spectra from SAR, WW3 and buoys show quite striking disagreement as shown in Figure 8(d). At low wavenumber, average of SAR MACS still displays the abrupt increase, while WW3 and buoy are in good agreement with weak spectral energy. Towards the higher wavenumber, all show a decreasing trend but with different spectral level. In particular, WW3 has the highest MACS values and buoy has the lowest. SAR lies in the middle and has comparable MACS with buoy for waves shorter than 60 m. The differing MACS between WW3 and buoy contrasts the alignment of one-dimensional wave spectra in Figure 8(a). This indicated that the directional pattern of both wave spectra might be different. To confirm, the mean wave direction as well as the spectral spread for both wind sea and swell part are calculated. The partition of wind sea from swell is based on the assumption of a fully developed sea state where the wind and waves are in equilibrium. The separation wavenumber k_s is set as the wavenumber where its phase speed equates the local wind speed. The mean wave direction and the directional spread are then computed in terms of the following formulas (Herbers et al., 1999)

$$tan\phi_m = \frac{\int_{k_0}^{k_1} \int_{-\pi}^{\pi} sin\phi S(k,\phi) dk d\phi}{\int_{k_0}^{k_1} \int_{-\pi}^{\pi} cos\phi S(k,\phi) dk d\phi} \tag{4}$$

and

$$\sigma_\phi^2 = \frac{\int_{k_0}^{k_1} \int_{-\pi}^{\pi} sin^2(\phi - \phi_m) S(k, \phi) dk d\phi}{\int_{k_0}^{k_1} \int_{-\pi}^{\pi} S(k, \phi) dk d\phi} \tag{5}$$

where k is the wavenumber and ϕ is the wave direction. For the wind sea, $k_0 = k_s$ and for the swell part, $k_1 = k_s$. $S(k, \phi)$ is the two-dimensional wave spectra from WW3 hindcast or the buoy measurements.

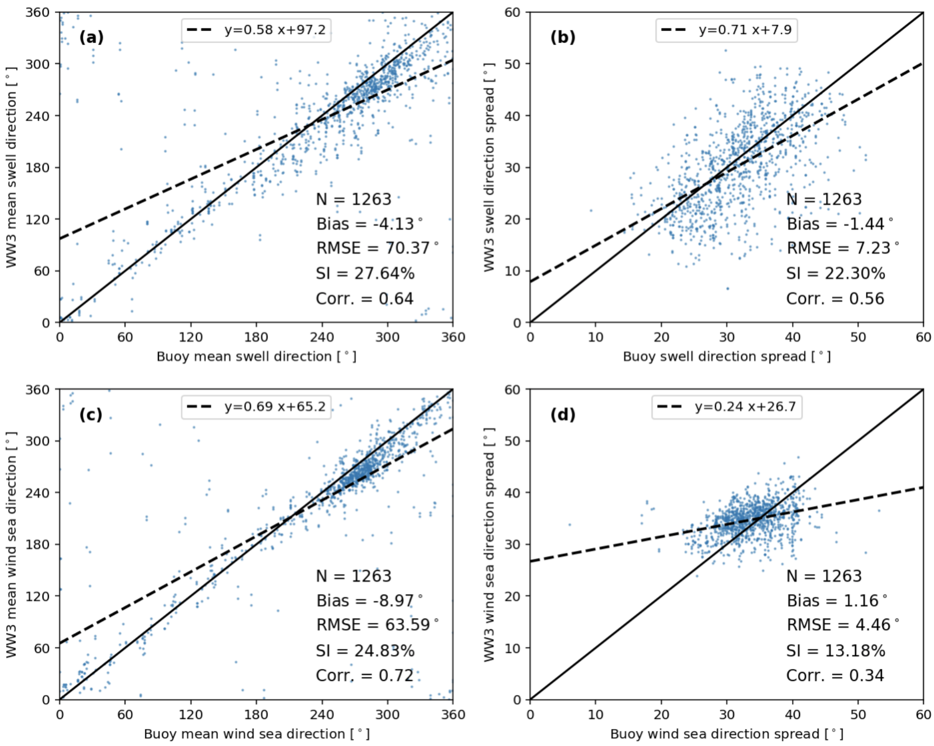

Figure 9: Comparison of mean wind sea in (a) and swell direction in (c) between WW3 outputs and buoy measurements with the directional spread accordingly shown in (b) and (d). Metrics are annotated on the bottom right.

The calculated mean wave direction and directional spread for both wind sea and swell part are presented in Figure 9. As reflected by the metrics, WW3 and buoy wave spectra are well matched for the swell waves. The mean wave direction of both data sets scatter tightly around the one-to-one line as shown in Figure 9(a). While the swell direction spreads appears to loose relationship with large standard deviation in comparison to the magnitude. By comparison, bias of the mean wind sea direction in Figure 9(c) is -8.97°, which is larger than that of the wave direction. Though bias of the spectral spread for wind sea is small of 1.16° (Figure 9(d)), the lower correlation coefficient of 0.34 suggests that these two are not well related. In fact, the linear slope of least-squared fit to these points is 0.24, which is much smaller compared to the 0.71 for swell waves in Figure 9(b). The impact of wind sea on the simulated MACS profile is two-fold. One one hand, the slightly shifted wind sea direction might result in differing MACS magnitude along the range direction. On the other hand, the wind sea spread could cause the nonlinear velocity bunching to be different between buoy and WW3 cases. This would accordingly change the magnitude of SAR image spectra as well as the MACS.

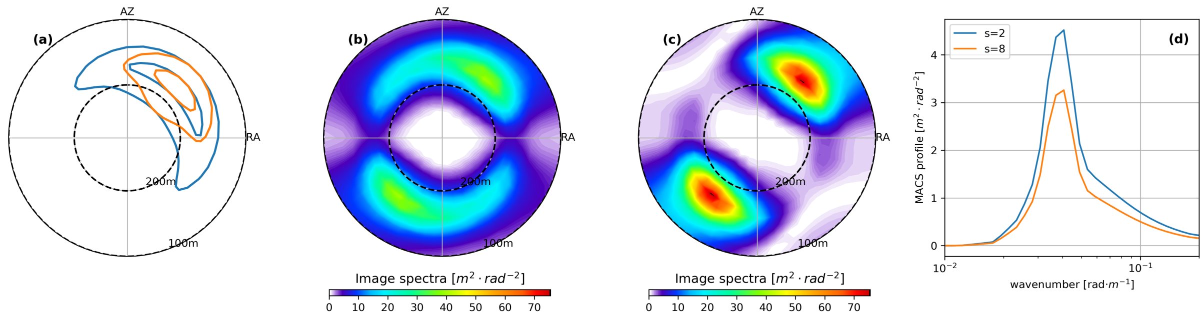

Figure 10: (a) The normalized directional wave spectrum for $s = 2$ (blue curve) and $s = 8$ (orange curve) in Eq. (6). The contour lines give the 25% and 75% relative to the maximum spectral energy. The simulated SAR image cross-spectrum is given in (b) $s = 2$ and (c) $s = 8$, respectively. (d) The accordingly extracted MACS profile.

To demonstrate this assumption, two SAR cross-spectra are simulated based on the JONSWAP spectrum and the following directional spreading function (Mitsuyasu et al., 1975):

$$D(k, \phi) = \left|cos[(\phi - \bar{\phi})/2]\right|^{(2s)} \tag{6}$$

where ϕ is the wave direction and $\bar{\phi}$ denotes the dominant wave direction. The parameter s determines the concentration degree of the spreading function relative to the mean direction. For simplicity, two constant values of $s = 2$ and $s = 8$ are set to calculate the directional wave spectra as shown in Figure 10 (a). The contour lines represent the 25% and 75% of the maximum wave spectral energy, respectively. The mean wave direction is 45° from the azimuth, the wind speed is $8m \cdot s^{-1}$ and the wind fetch is 500 km. The wave spectrum of $s = 2$ (blue curve) displays wider spread compared to that of $s = 8$ (orange curve). The combination effect of wave direction deviation from the range axis and the wider spread function for $s = 2$ results in larger wave spectra magnitude along the radar line-of-sight. In consequence, the simulated image spectra of $s = 2$ shown in Figure 10 (c) is larger than that of $s = 8$ in Figure 10 (b) in the range direction. This corresponds to the higher MACS profile simulated based on the wide-spread wave spectrum (blue curve) as given in Figure (d). Note that the configuration of mean wave direction is similar to that of the mean wind sea direction in Figure 9. The results that larger direction spread yields higher MACS profile, in accordance with the slightly greater wind sea direction spread in Figure 9(d), to some extend explain the MACS comparison in Figure 8(d). Further in-depth and comprehensive evaluation of WW3 outputs relative to the buoy measurements in terms of the spectral perspective, rather than the integrated wave height should be devised.

4. Discussion

As a parameter defined relative to variable wavelengths, MACS offers new perspectives to make comparisons between SAR observations and the reference data produced by WW3. In general, the global patterns of SAR-observed MACS promisingly resemble that of the WW3-simulation. Yet the quantitative disagreements are noticeable. As demonstrated by the percentile analyses of MACS profile in Figure 2, SAR and WW3 have particularly marked difference for long waves (wavelength longer than 300 m) and wind sea (wavelength shorter than 100 m). The MACS overestimation of wind sea relative to the WW3-simulation is consistent on the globe as shown in Figure 5(a). While the difference for long waves is region dependent as in Figure 5(c). As illustrated in Figure 1, the long waves derived from SAR images are subject to impact of atmospheric and/or oceanic features on the sea surface, which pollutes the wave signals in the MACS analyses. In fact, the influence of large-scale features on radar backscatter also depends on the local wind speed. As concluded in (Wang et al., 2019), the rain is hard to detect at high winds. As such, its impact on the spectra at long wavelength is negligible so that $\mathrm{MACS}_{342.0}$ has consistent values for both R1 and R3 regions in the Southern extratropics. While for R2 at low winds, SAR-observed $\mathrm{MACS}_{342.0}$ is much higher as shown in Figure 7(b3).

A test is performed as a first attempt to illustrate the impact of other phenomena on MACS estimates. In general, SAR image spectra of these patterns have an unusually high tail at low wavenumber of MACS profile similar to that in Figure 1(d4). A simple criteria is employed to

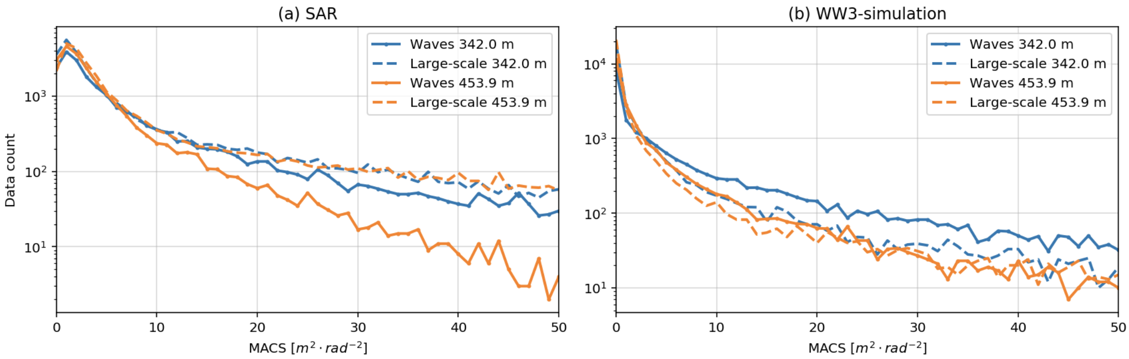

Figure 11: Histogram of (a) SAR and (b)WW3-simulated MACS$_{342.0}$ and MACS$_{453.9}$ with (dashed curves) and without (solid curves) potential impact of large-scale features on SAR images.

sort out the cases with such high-tail form. If the averaged MACS for wavelengths longer than 342.0 m is larger than its counterpart for shorter wavelengths (<342.0 m), this case is assumed to be impacted by the large-scale features. Otherwise, ocean wave signatures are expected to be dominant in this case. The histogram of MACS for two wavelengths of 342.0 m and 453.9 m is presented in Figure 11. For SAR-measured MACS in Figure 11(a), all cases with large-scale features tend to have larger MACS magnitude in comparison to the dominant waves. The two curves of MACS$_{342.0}$ (blue) are closer to each other in comparison to those of MACS$_{453.9}$ (orange). This is indicative of the enlarging impact of these large-scale features with wavelengths. While WW3 wave spectra are only able to predict surface wave properties, the MACS contrast between the pure waves (solid line) and potential large-scale (dashed) in Figure 11(b) is not as evident as that in Figure 11(a). Given the non-negligible different shown in Figure 11(a), processing procedure is essential to identify the presence of large-scale phenomena and filter out their contributions in the SAR image spectrum for a proper interpretation of the image cross-spectra. As a matter of fact, on-going efforts are being made to classify these features based on a deep learning technique for Sentinel-1 observations. Valid algorithms are expected to be deployed and a consistent reprocessing from ASAR to Sentinel-1 shall then be feasible for improved wave measurements.

5. Summary

Spaceborne SAR has been proven to be an advantageous sensor in global wave observations (Hasselmann et al., 2012). Despite the previously extended study to evaluate SAR wave observations based on the subrange wave height (Li and Saulter, 2012), the capability of SAR mapping isolated wave component remains undisclosed. This study further advances the SAR wave validation towards the image spectral level through the newly defined MACS parameter. One of its advantages is its versatility, allowing the comparison to be directly made for various wavelengths without the complicated SAR inversion scheme.

The large volume of data acquired by Envisat/ASAR aids the examination of MACS relationships with respect to the collocated WW3 hindcast wave spectra. Both data sets show a couple of similarities in MACS signatures. First of all, MACS magnitudes of all wavelengths are comparable between SAR observation and WW3-simulation. The global patterns of SAR and WW3 derived MACS agree well with high correlations in the open ocean. However, the quantitative inconsistency between these two is not only wavelength variant, but also regionally dependent. WW3 appears to constantly predict larger MACS magnitude for short wavelength (<100 m) at global scale. For long waves (>300 m), such overestimate by WW3 only exhibits in the southern extratropics with opposite trend in the trade winds where WW3 predicts consistently smaller values. In contrast to the well aligned significant wave height (Li and Saulter, 2012; Stopa and Mouche, 2017), the difference observed by MACS of various wave scales is expected to offer new insights into the assessment approach of SAR observations.

Even with the assumption that SAR forward transformation used in this paper is able to accurately reproduce the wave imaging process, several points still need to be addressed in order to better interpret the results of MACS comparison. On one hand, the large-scale impact should be further quantified as effort to isolate the MACS quantity that is associated with ocean surface waves. This will in turn help refine the SAR wave inversion and further enhance the utility of SAR measurements to infer the realistic ocean swell partitions. In addition, other geophysical applications, such as air-sea interactions and sea ice monitoring shall also benefit. On the other hand, the spectral spread has been demonstrated to have impact on the MACS magnitude along with the mean wave direction. The inconsistency observed between buoy-based and WW3-based simulations also invokes the necessity of validating the numerical outputs in terms of the two-dimensional wave spectra rather than the integrated parameters.

In this paper, we focused on the assessment of MACS profile from the Envisat/ASAR wave mode observations. There are also multiple SAR sensors in orbit now, including Sentinel-1 constellation, Radarsat Constellation Mission, Gaofen-3 et al. Instrument characteristics, such as spatial resolution, swath and incidence angles, generally differ among these satellites. While the commonly used validation procedure through significant wave height is limited to evaluate the SAR wave measurements. This MACS approach can be readily extended to grade the performance of SAR observations from the spectral point of view as well as to determine the consistency between sensors.

6. Acknowledgments

This study is supported in part by the National Science Foundation of China (under grant 42006163, 42027805, 42076181 and 41620104003), in part by the Startup Foundation for Introducing Talent of NUIST, in part by the European Space Agency under grant of Sentinel-1 Mission Performance Center (Contract No. 4000107360/12/I-LG) and S1-4SCI Ocean Study project (Contract No. 4000115170/15/I-SBo), in part by the Centre National D'études Spatiales (TOSCA program, COWS project). The ECMWF reanalysis winds are obtained in the framework of Sentinel-1 Mission Performance Center and are publicly available (ecmwf.int). The wave buoy data are provided by NDBC and publicly available via .

References

Ardhuin, F., Rogers, E., Babanin, A.V., Filipot, J.F., Magne, R., Roland, A., van der Westhuysen, A., Queffeulou, P., Lefevre, J.M., Aouf, L., et al., 2010. Semiempirical dissipation source functions for ocean waves. part i: Definition, calibration, and validation. Journal of Physical Oceanography 40, 19171941. URL: http://dx.doi.org/10.1175/2010JPO4324.1, doi:10.1175/2010jpo4324.1.

Ardhuin, F., Stopa, J., Chapron, B., Collard, F., Smith, M., Thomson, J., Doble, M., Blomquist, B., Persson, O., Collins, C.O., Wadhams, P., 2017. Measuring ocean waves in sea ice using sar imagery: A quasi-deterministic approach evaluated with sentinel-1 and in situ data. Remote Sensing of Environment 189, 211 – 222. URL: http://www.sciencedirect.com/science/article/pii/S0034425716304710, doi:https://doi.org/10.1016/j.rse.2016.11.024.

Collard, F., Ardhuin, F., Chapron, B., 2009. Monitoring and analysis of ocean swell fields from space: New methods for routine observations. Journal of Geophysical Research: Oceans 114, 1–15. URL: https:

//agupubs.onlinelibrary.wiley.com/doi/abs/10.1029/2008JC005215, doi:10.1029/2008JC005215, arXiv:https://agupubs.onlinelibrary.wiley.com/doi/pdf/10.1029/2008JC005215.

Engen, G., Johnsen, H., 1995. Sar-ocean wave inversion using image cross spectra. IEEE Transactions on Geoscience and Remote Sensing 33, 1047–1056. doi:10.1109/36.406690.

Hasselmann, K., Barnett, T., Bouws, E., Carlson, H., Cartwright, D., Enke, K., Ewing, J., Gienapp, H., Hasselmann, D., Kruseman, P., Meerburg, A., Mller, P., Olbers, D., Richter, K., Sell, W., Walden, H., 1973. Measurements of wind-wave growth and swell decay during the Joint North Sea Wave Project (JONSWAP). Part of collection: Hydraulic Engineering Reports A(8), 12. Deutches Hydrographisches Institut. Hamburg, Germany.

Hasselmann, K., Chapron, B., Aouf, L., Ardhuin, F., Collard, F., Engen, G., Hasselmann, S., Heimbach, P., Janssen, P., Johnsen, H., Krogstad, H., Lehner, S., Li, J.G., Li, X.M., Rosenthal, W., Schulz-Stellenfleth, J., 2012. The ers sar wave mode – a breakthrough in global ocean wave observations. URL: https://elib.dlr.de/77565/.

Hasselmann, S., Hasselmann, K., 1985. Computations and parameterizations of the nonlinear energy transfer in a gravity-wave spectrum. part i: A new method for efficient computations of the exact nonlinear transfer integral. Journal of Physical Oceanography 15, 1369–1377. URL: https://doi.org/10.1175/1520-0485(1985)015<1369:CAPOTN>2.0.CO;2, doi:10.1175/1520-0485(1985)015<1369:CAPOTN>2.0.CO;2, arXiv:https://doi.org/10.1175/1520-0485(1985)015<1369:CAPOTN>2.0.CO;2.

Herbers, T.H.C., Elgar, S., Guza, R.T., 1999. Directional spreading of waves in the nearshore. Journal of Geophysical Research: Oceans 104, 7683–7693. URL: https://agupubs.onlinelibrary.wiley.com/doi/abs/10.1029/1998JC900092, doi:10.1029/1998JC900092, arXiv:https://agupubs.onlinelibrary.wiley.com/doi/pdf/10.1029/1998JC900092.

Johnsen, H., 2005. ENVISAT ASAR Wave Mode Product Description and Reconstruction Procedure. Technical Report 1/2005. Norut. Tromso, Norway.

Kerbaol, V., Chapron, B., Vachon, P.W., 1998. Analysis of ERS-1/2 synthetic aperture radar wave mode imagettes. Journal of Geophysical Research: Oceans 103, 7833–7846. doi:10.1029/97jc01579.

Krogstad, H.E., Samset, O., Vachon, P.W., 1994. Generalizations of the nonlinear oceansar transform and a simplified sar inversion algorithm. Atmosphere-Ocean 32, 61–82. URL: https://doi.org/10.1080/07055900.1994.9649490, doi:10.1080/07055900.1994.9649490, arXiv:https://doi.org/10.1080/07055900.1994.9649490.

Li, H., Chapron, B., Mouche, A., Stopa, J.E., 2019. A new ocean sar cross-spectral parameter: Definition and directional property using the global sentinel-1 measurements. Journal of Geophysical Research: Oceans 124, 1566–1577. URL: https://agupubs.onlinelibrary.wiley.com/doi/abs/10.1029/2018JC014638, doi:10.1029/2018JC014638, arXiv:https://agupubs.onlinelibrary.wiley.com/doi/pdf/10.1029/2018JC014638.

Li, H., Mouche, A., Wang, H., Stopa, J.E., Chapron, B., 2019. Polarization dependence of azimuth cutoff from quadpol sar images. IEEE Transactions on Geoscience and Remote Sensing , 1–10doi:10.1109/TGRS.2019.2929835.

Li, J.G., Saulter, A., 2012. Assessment of the updated Envisat ASAR ocean surface wave spectra with buoy and altimeter data. Remote Sensing of Environment 126, 72–83. doi:10.1016/j.rse.2012.08.018.

Lygre, A., Krogstad, H.E., 1986. Maximum entropy estimation of the directional distribution in ocean wave spectra. Journal of Physical Oceanography 16, 2052–2060. URL: https://doi.org/10.1175/1520-0485(1986)016<2052:MEEOTD>2.0.CO;2, doi:10.1175/1520-0485(1986)016<2052:MEEOTD>2.0.CO;2, arXiv:https://doi.org/10.1175/1520-0485(1986)016<2052:MEEOTD>2.0.CO;2.

Mitsuyasu, H., Tasai, F., Suhara, T., Mizuno, S., Ohkusu, M., Honda, T., Rikiishi, K., 1975. Observations of the Directional Spectrum of Ocean WavesUsing a Cloverleaf Buoy. Journal of Physical Oceanography 5, 750–760. URL: https://doi.org/10.1175/1520-0485(1975)005<0750:OOTDSO>2.0.CO;2, doi:10.1175/1520-0485(1975)005<0750:OOTDSO>2.0.CO;2, arXiv:https://journals.ametsoc.org/jpo/article-pdf/5/4/750/4603070/1520-0485(1975)005_0750_ootdso_2_

Nagarajan, B., Aiyyer, A.R., 2004. Performance of the ecmwf operational analyses over the tropical indian ocean. Monthly Weather Review 132, 2275–2282. URL: https://doi.org/10.1175/1520-0493(2004)132<2275:POTEOA>2.0.CO;2, doi:10.1175/1520-0493(2004)132<2275:POTEOA>2.0.CO;2, arXiv:https://doi.org/10.1175/1520-0493(2004)132<2275:POTEOA>2.0.CO;2.

Quach, B., Glaser, Y., Stopa, J.E., Mouche, A.A., Sadowski, P., 2020. Deep learning for predicting significant wave height from synthetic aperture radar. IEEE Transactions on Geoscience and Remote Sensing , 1–9doi:10.1109/TGRS.2020.3003839.

Queffeulou, P., 2004. Long-term validation of wave height measurements from altimeters. Marine Geodesy 27, 495–510. URL: https://doi.org/10.1080/01490410490883478, doi:10.1080/01490410490883478, arXiv:https://doi.org/10.1080/01490410490883478.

Saha, S., Moorthi, S., Pan, H.L., Wu, X., Wang, J., Nadiga, S., Tripp, P., Kistler, R., Woollen, J., Behringer, D., Liu, H., Stokes, D., Grumbine, R., Gayno, G., Wang, J., Hou, Y.T., Chuang, H.y., Juang, H.M.H., Sela, J., Iredell, M., Treadon, R., Kleist, D., Van Delst, P., Keyser, D., Derber, J., Ek, M., Meng, J., Wei, H., Yang, R., Lord, S., van den Dool, H., Kumar, A., Wang, W., Long, C., Chelliah, M., Xue, Y., Huang, B., Schemm, J.K., Ebisuzaki, W., Lin, R., Xie, P., Chen, M., Zhou, S., Higgins, W., Zou, C.Z., Liu, Q., Chen, Y., Han, Y., Cucurull, L., Reynolds, R.W., Rutledge, G., Goldberg, M., 2010. The ncep climate forecast system reanalysis. Bulletin of the American Meteorological Society 91, 1015–1058. URL: https://doi.org/10.1175/2010BAMS3001.1, doi:10.1175/2010BAMS3001.1, arXiv:https://doi.org/10.1175/2010BAMS3001.1.

Saha, S., Moorthi, S., Wu, X., Wang, J., Nadiga, S., Tripp, P., Behringer, D., Hou, Y.T., Chuang, H.y., Iredell, M., Ek, M., Meng, J., Yang, R., Mendez, M.P., van den Dool, H., Zhang, Q., Wang, W., Chen, M., Becker, E., 2014. The ncep climate forecast system version 2. Journal of Climate 27, 2185–2208. URL: https://doi.org/10.1175/JCLI-D-12-00823.1, doi:10.1175/JCLI-D-12-00823.1, arXiv:https://doi.org/10.1175/JCLI-D-12-00823.1.

Schulz-Stellenfleth, J., Knig, T., Lehner, S., 2007. An empirical approach for the retrieval of integral ocean wave parameters from synthetic aperture radar data. Journal of Geophysical Research: Oceans 112, 1–14. URL: https://agupubs.onlinelibrary.wiley.com/doi/abs/10.1029/2006JC003970, doi:10.1029/2006JC003970, arXiv:https://agupubs.onlinelibrary.wiley.com/doi/pdf/10.1029/2006JC003970.

Stopa, J.E., 2018. Wind forcing calibration and wave hindcast comparison using multiple reanalysis and merged satellite wind datasets. Ocean Modelling 127, 55–69. doi:10.1016/j.ocemod.2018.04.008.

Stopa, J.E., Ardhuin, F., Babanin, A., Zieger, S., 2016a. Comparison and validation of physical wave parameterizations in spectral wave models. Ocean Modelling 103, 2 – 17. URL: http://www.sciencedirect.com/science/article/pii/S1463500315001614, doi:https://doi.org/10.1016/j.ocemod.2015.09.003. waves and coastal, regional and global processes.

Stopa, J.E., Ardhuin, F., Husson, R., Jiang, H., Chapron, B., Collard, F., 2016b. Swell dissipation from 10years of envisat advanced synthetic aperture radar in wave mode. Geophysical Research Letters 43, 3423–3430. URL: https://agupubs.onlinelibrary.wiley.com/doi/abs/10.1002/2015GL067566, doi:10.1002/2015GL067566, arXiv:https://agupubs.onlinelibrary.wiley.com/doi/pdf/10.1002/2015GL067566.

Stopa, J.E., Ardhuin, F., Stutzmann, E., Lecocq, T., 2019. Sea state trends and variability: consistency between models, altimeters, buoys, and seismic data (1979-2016). Journal of Geophysical Research: Oceans , 3923–3940doi:10.1029/2018jc014607.

Stopa, J.E., Mouche, A., 2017. Significant wave heights from sentinel-1 sar: Validation and applications. Journal of Geophysical Research: Oceans 122, 1827–1848. URL: https://agupubs.onlinelibrary.wiley.com/doi/abs/10.1002/2016JC012364, doi:10.1002/2016JC012364, arXiv:https://agupubs.onlinelibrary.wiley.com/doi/pdf/10.1002/2016JC012364.

The WAVEWATCH III® Development Group, . User manual and system documentation of WAVEWATCH III® version 5.16. NOAA/NWS/NCEP/MMAB, College Park, MD, USA.

Žagar, N., Skok, G., Tribbia, J., 2011. Climatology of the itcz derived from era interim reanalyses. Journal of Geophysical Research: Atmospheres 116, 1–6. URL: https://agupubs.onlinelibrary.wiley.com/doi/abs/10.1029/2011JD015695, doi:10.1029/2011JD015695, arXiv:https://agupubs.onlinelibrary.wiley.com/doi/pdf/10.1029/2011JD015695.

Vandemark, D., Chapron, B., Elfouhaily, T., Campbell, J.W., 2005. Impact of highfrequency waves on the ocean altimeter range bias. Journal of Geophysical Research: Oceans 110. URL: https://agupubs.onlinelibrary.wiley.com/doi/abs/10.1029/2005JC002979, doi:10.1029/2005JC002979, arXiv:https://agupubs.onlinelibrary.wiley.com/doi/pdf/10.1029/2005JC002979.

Wang, C., Tandeo, P., Mouche, A., Stopa, J.E., Gressani, V., Longepe, N., Vandemark, D., Foster, R.C., Chapron, B., 2019. Classification of the global sentinel-1 sar vignettes for ocean surface process studies. Remote

Sensing of Environment 234, 111457. URL: http://www.sciencedirect.com/science/article/pii/S0034425719304766, doi:https://doi.org/10.1016/j.rse.2019.111457.

Young, I., 1999. Seasonal variability of the global ocean wind and wave climate. International Journal of Climatology 19, 931–950. URL: https://rmets.onlinelibrary.wiley.com/doi/abs/10.1002/%28SICI%291097-0088%28199907%2919%3A9%3C931%3A%3AAID-JOC412%3E3.0.CO%3B2-O, doi:10.1002/(SICI)1097-0088(199907)19:9<931::AID-JOC412>3.0.CO;2-O, arXiv:https://rmets.onlinelibrary.wiley.com/doi/pdf/10.1002/%28SICI%291097-0088%28199907%2919%3A9%3

Young, I.R., Zieger, S., Babanin, A.V., 2011. Global trends in wind speed and wave height. Science 332, 451–455. URL: http://science.sciencemag.org/content/332/6028/451, doi:10.1126/science.1197219, arXiv:http://science.sciencemag.org/content/332/6028/451.full.pdf.

Zieger, S., Vinoth, J., Young, I.R., 2009. Joint calibration of multiplatform altimeter measurements of wind speed and wave height over the past 20 years. Journal of Atmospheric and Oceanic Technology 26, 2549–2564. URL: https://doi.org/10.1175/2009JTECHA1303.1, doi:10.1175/2009JTECHA1303.1, arXiv:https://doi.org/10.1175/2009JTECHA1303.1.